J. Fluid Mech. (2023), *vol*. 974, A12, doi:10.1017/jfm.2023.806

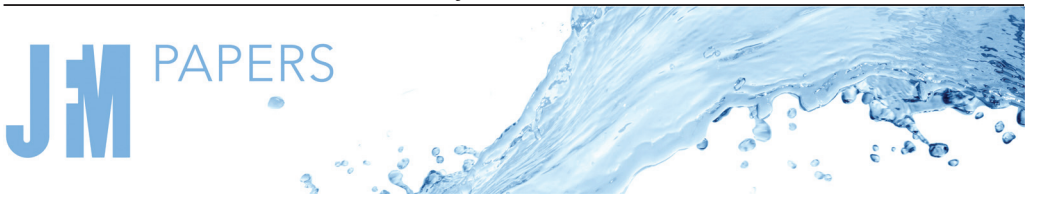

Gap-modulated dynamics of flexible plates

Shyuan Cheng[1], **Stefano Olivieri**[2,3], **Marco E. Rosti**[3] and **Leonardo P. Chamorro**[1,4,5,6,†]

[1]Mechanical Science and Engineering, University of Illinois, Urbana, IL 61801, USA

[2]Aerospace Engineering, Universidad Carlos III de Madrid, 28911 Leganés, Spain

[3]Complex Fluids and Flows Unit, Okinawa Institute of Science and Technology Graduate University, Okinawa 904-0495, Japan

[4]Aerospace Engineering, University of Illinois, Urbana, IL 61801, USA

[5]Geology, University of Illinois, Urbana, IL 61801, USA

[6]Civil and Environmental Engineering, University of Illinois, Urbana, IL 61801, USA

(Received 9 March 2023; revised 9 August 2023; accepted 19 September 2023)

The effect of single perforations and their location on the drag and reconfiguration of flexible plates was explored through laboratory experiments and direct numerical simulations. The plates were subjected to uniform flows with negligible turbulence, and the perforations had a square cross-section resulting in a low porosity ratio of $\gamma \approx 0.028$. Rigid plates with and without perforations and flexible plates without perforations served as the baseline cases. The perforated plates exhibited distinct jets through the openings in the wake, significantly impacting the aerodynamic force and plate deformation. The velocity and position of the centre jet velocity in relation to downwind distance were influenced by both the incoming flow and the location of the perforations. The centre jet velocity profiles were normalized using an effective velocity and corrected perforation half-width, revealing their dependence on these factors. A simple first-order formulation was developed to predict the change in drag for various perforated plates under a wide range of incoming velocities. This formulation was supported by numerical simulations across a wider range of Cauchy number to confirm the proposed model and separate the effect of the Cauchy and Reynolds numbers. The results of this study may inform the design of flexible structures, define effective porosity and serve as an initial step towards modelling the complex interaction between flow and structures with low porosity.

Key words: flow–structure interactions

† Email address for correspondence: lpchamo@illinois.edu

1. Introduction

Characterizing the flow-induced reconfiguration of flexible structures has been the subject of intense research due to its relevance in various engineering, biological and environmental fields (Taylor 1952; Harder *et al.* 2004; Vollsinger *et al.* 2005; Stanford *et al.* 2008; Vogel 2009). Flexible structures experience reduced drag, D, compared with their rigid counterparts (Vogel 1984; Alben, Shelley & Zhang 2002, 2004; Gosselin, De Langre & Machado-Almeida 2010; Luhar & Nepf 2011; Leclercq & de Langre 2016; Hong *et al.* 2022) due to deformation into streamlined shape, thus reducing the frontal area. This leads to changes in the typical drag's quadratic dependence with incoming flow velocity U_0 in rigid bodies at sufficiently high Reynolds number, resulting in $D \propto U_0^{2+V}$, where $V < 0$ generally, is the so-called Vogel exponent. Evidence shows that the Vogel exponent depends on various parameters, including the geometry and material of the structure, buoyancy, skin friction and incoming flow mean shear. Alben *et al.* (2002, 2004) showed that plates deform into quasiparabolic shapes when subjected to high flow velocity and found a Vogel exponent of $V \approx -0.67$. Gosselin *et al.* (2010) investigated the drag of two flexible object geometries subjected to a wide range of incoming velocity; they showed that the data can be collapsed to a single curve when normalized by a scale Cauchy number and the flexible object deformation also collapse to a quasiparabolic curve. Luhar & Nepf (2011) explored the role of blade stiffness and buoyancy on blade reconfiguration and proposed a model for drag and reconfiguration applicable to seagrass and microalgae in natural settings. Their model quantifies the degree of reconfiguration as a function of two dimensionless ratios: the Cauchy number, Ca, defined as drag to stiffness restoring force ratio; and the ratio between restoring force caused by buoyancy and stiffness-related restoring force.

Porous structures are paramount in various engineering systems and frequently encountered in nature; examples include coral groups, insect wings and seeds. Their ability to control aero- and hydrodynamic forces by modulating the degree of reconfiguration and the surrounding flow has been studied over the last decades (Tunnicliffe 1982; Santhanakrishnan *et al.* 2014; Cummins *et al.* 2018; Farisenkov *et al.* 2020). Most studies have focused on rigid perforated bodies and showed that the drag coefficient decreases as the structure porosity increases (Guan, Zhang & Zhu 2003; Bitog *et al.* 2011; Basnet & Constantinescu 2017). Dong *et al.* (2007, 2010) also demonstrated that structure porosity affects the flow in the vicinity of a porous plate, which leads to a reduction of recirculation in the wake. Lee & Kim (1999) and Basnet & Constantinescu (2017) reported a lack of recirculation region immediately behind the porous plate if the porosity, γ, is sufficiently high ($\gamma \geq 35\,\%$). Recently, Singh & Narasimhamurthy (2022) performed direct numerical simulations on the wake of uniformly perforated plates and showed that the bleed-through perforation is the main reason for drag reduction. The onset of periodic Kármán vortex shedding was first noted by Castro (1971), who observed a critical porosity level for Reynolds numbers within the range of $2.5 \times 10^4 < Re < 9 \times 10^4$. Numerous studies have examined the relationship between drag coefficient and porosity dependence, with pressure loss being influenced by several parameters such as Reynolds number (Re), porosity ratio (γ) and Mach number (Ma). Early models formulated by Betz (1920) proved helpful in a particular range of porosities but underestimated the drag coefficient at relatively low porosities. A model proposed by Koo & James (1973) scaled the wake velocity to match the boundary conditions but also underestimated drag at low porosity. Steiros & Hultmark (2018) incorporated the impact of base suction, leading to improved drag predictions at low porosity.

Compared with their rigid counterpart, the interaction between flow and flexible porous structures has not been explored in detail. Guttag *et al.* (2018) investigated the influence

of base clamping on the static deformation of perforated plates. Recent work by Jin *et al.* (2020) explored the mean drag, wake and reconfiguration of structure with various degrees of uniform porosity. They showed the possibility of a positive Vogel exponent for a sufficiently high porosity level, which was explained by a relatively high effective velocity near the structure. Despite the efforts to characterize the impact of porosity on flexible structures, these investigations solely considered uniform porosity over the plate. As a result, the effects of localized porosity and the influence of spatially distributed perforations on mean drag and deformation have been overlooked and remain mostly unexplored.

This study explores the impact of localized perforations on plate deformation and forces. We employ a combination of wind-tunnel experiments and direct numerical simulations to examine a wide range of parameters and gain valuable insights into the reconfiguration of plates. Section 2 provides detailed information about the experimental set-up, and § 3 discusses the main results. Finally, § 4 summarizes the key findings of the study.

2. Experimental set-up

The experiments were conducted in the Eiffel-type wind tunnel at the Talbot Laboratory of the University of Illinois. The wind tunnel is characterized by a test section of 6.10 m in length, 0.91 m in width and 0.45 m in height. The tunnel ceiling is adjustable to impose pressure gradients set to nearly zero along the test section.

We explored the reconfiguration of flexible plates with a single square perforation at different heights along their vertical axis. Square orifices, as canonical shapes, offer a comparatively simple method for characterization in relation to rectangular plates. Also, they complement research in various applications (e.g. Ibrahim *et al.* 2020). The plates had identical characteristics, namely, length $L = 200$ mm, width $b = 50$ mm, thickness $c = 0.38$ mm, Young's modulus $E = 2.4$ GPa and density $\rho = 1180\ \mathrm{kg\ m^{-3}}$. The perforation had a side length of $a = b/3 = 16.7$ mm, resulting in a porosity ratio of $\gamma = a^2/(bL) \approx 0.028$. We tested the plates with single perforations at 11 positions along the vertical axis, with the perforation centred at $y/L = (2n-1)/24$ for $n = 1, \ldots, 11$. Hereafter, we use the nomenclature $P1$ to $P11$ to refer to the perforated plates, where $P1$ denotes the plate with the perforation at the base, and $P11$ refers to the plate with the perforation nearest to the tip. The solid plate without perforation is denoted by $P0$; see schematic in figure 1. Basic parameters, including the global and local coordinate systems, the local bending angle at perforation θ and an arclength s, are illustrated in figure 1(*b*). The global coordinate has the origin at the root of the plates, with x and y in the streamwise and wall-normal direction, whereas the local coordinate origin (x_0, y_0) is set at the centre of the perforation and also points towards the streamwise and vertical directions, and $s = 0$ is at the root of the plate. We also examined selected rigid plates with perforations at three locations ($P4$, $P7$ and $P11$) and the base cases with rigid and flexible plates without perforations ($P0$), which also served as a reference.

Although porosity could affect the plates' structural characteristics, the equivalent bending stiffness EI_{eq} and mass per unit length $\rho_m A_{eq}$ only underwent minor changes. Following Luschi & Pieri (2014) and Barry & Tanbour (2018), these are given by

$$\left.\begin{aligned} \rho_m A_{eq} &= \frac{\rho_m bc(1 - N(\gamma - 2))\gamma}{N + \gamma}, \\ EI_{eq} &= EI\frac{(N+1)\gamma(N^2 + 2N + \gamma^2)}{(1-\gamma^2+\gamma^3)N^3 + 3\gamma N^2 + (3 + 2\gamma - 3\gamma^2 + \gamma^3)\gamma^2 N + \gamma^3}. \end{aligned}\right\} \tag{2.1}$$

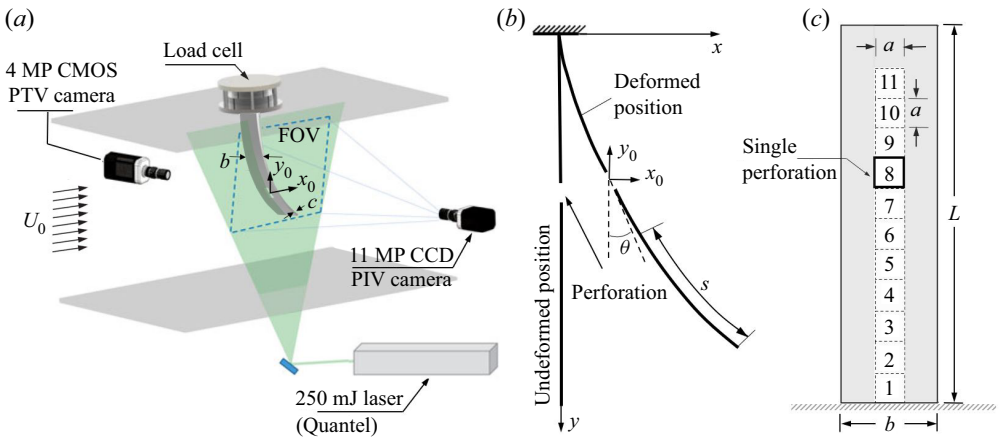

Figure 1. (*a*) Basic schematic of the experimental set-up (not scaled) illustrating the load cell, field of view (FOV), local horizontal-vertical coordinate (x_0, y_0) with origin at the centre of the perforation, (*b*) schematic of a plate illustrating arclength, s, and the local bending angle at perforated location, θ, and (*c*) locations of the single perforations in the plate.

Here, $I = bc^3/12$ is the second moment of area and $N = 1$ for single perforation. From (2.1), the variation results in less than 3 % compared with the base case without perforation. Additionally, the aspect ratio of the plate, $L/b = 4$ and $L/c \gg 100$, minimizes the influence of the Poisson ratio (Jin *et al.* 2020).

The plates were affixed perpendicular to the top wall of the tunnel and oriented to face the incoming flow at the start of the tunnel test section, where the boundary layer was considered negligible. The gravitational and elastic restoring forces ratio, $G = \Delta\rho g b c L^3/(EI) \approx 3.76$ (Luhar & Nepf 2011; Jin *et al.* 2020), show some gravitational effect on the plate deformation. We characterized the aerodynamic force and reconfiguration of each plate at 16 incoming velocities, U_0, ranging from 2 to 10 m s^{-1} at intervals of $\Delta U_0 = 0.5$ m s^{-1}. This resulted in a Reynolds number range of $Re = U_0 b/\nu \in [6.8, 33.8] \times 10^3$, where ν denotes the kinematic viscosity of air, and Cauchy numbers $Ca = \rho_f b L^3 U_0^2/(EI) \in [3.8, 94.5]$, where $\rho_f = 1.293$ Kg m^{-3} is the density of air. Note that, for the conditions under analysis, the flow can be described as incompressible, indicated by a Mach number $Ma < 0.03$.

A high-resolution ATI Gamma load cell was utilized to measure the aerodynamic forces accurately and torques at a sampling rate of 1 kHz for 90 s. Each force measurement was repeated thrice, resulting in a total measurement time of 270 s for each case. The minimum drag scenario had an uncertainty of approximately 3 % (Jin *et al.* 2020). To capture the deformation and vibration of the plates, a two-dimensional particle tracking velocimetry (PTV) technique was employed on 20 fiducial points equally distributed on the side of each acrylic plate. These fiducial points were illuminated by a halogen spotlight and captured using a 4 MP (2560 × 1600 pixel) Phantom M340 camera at a frequency of 100 Hz for duration of 30 s as shown in figure 1(*a*).

The flow field around the plates was characterized using particle image velocimetry (PIV). Two FOVs intersected at the centre of the plates were oriented perpendicularly to the wall and partially overlapped to produce a combined area of 225 mm × 700 mm. The flow was seeded with 1 µm olive oil droplets and illuminated by a 1 mm thick laser sheet created by a Quantel laser with a pulse energy of 250 mJ. A 4 MP CMOS camera captured 2400 image pairs of the FOVs at a frequency of 10 Hz.

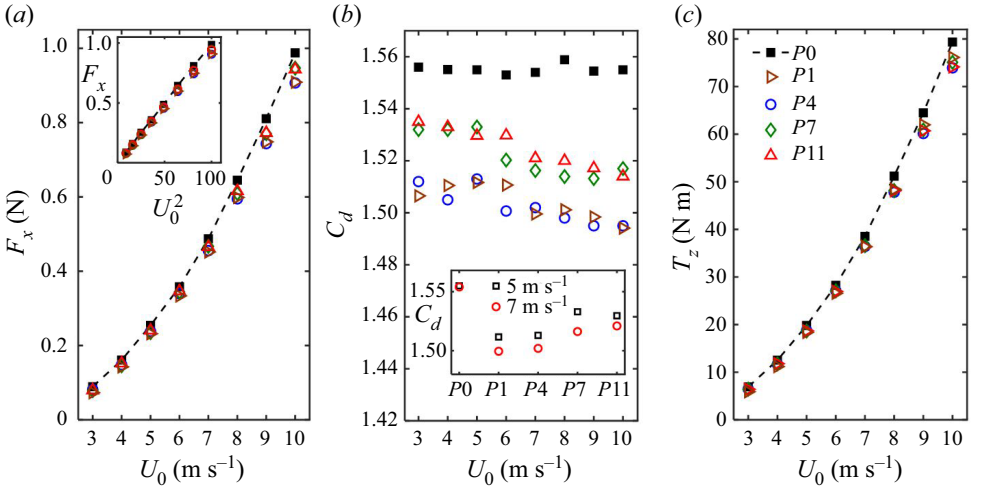

Figure 2. (*a*) Mean drag, F_x, (*b*) drag coefficient, C_d, and (*c*) main torque, T_z, of rigid perforated plates for various perforation locations: *P*1 (brown ▷); *P*4 (blue ○); *P*7 (green ◇); *P*11 (red △); and incoming velocities. The solid *P*0 (■) plate is included as a reference, and the inset shows C_d variation for various plates for a fixed U_0.

The images were analysed using TSI Insight 4G software with a recursive cross-correlation method and an interrogation window size of 24 × 24 pixel with 50 % overlap, resulting in a final vector grid spacing of $\Delta x = \Delta y = 1.68$ mm. The measurements were taken after the system reached a steady state, and a waiting period of at least 60 s was observed to minimize the initial transient effect.

3. Results

3.1. *Baseline assessment: mean aerodynamic force of rigid plates*

Figure 2 depicts the correlation between the flow velocity, the measured drag and the principal torque of the *P*0 (solid), *P*4, *P*7 and *P*11 rigid plates. The base plate without perforation follows the U_0^2 trend, illustrated as a dashed line. The plates with perforation display a lower level of drag and a marginal deviation from the quadratic pattern, as anticipated. The drag coefficient C_d is defined by

$$C_d = F_x/(\tfrac{1}{2}\rho_f U_0^2 A), \tag{3.1}$$

where A is the frontal area that accounts for the perforation. The rigid perforated plates exhibit a lower drag coefficient than the unperforated base plate, as illustrated in figure 2(*b*). This can be attributed to the jet that penetrates the wake of the cantilever plate. Notably, the *P*1 and *P*4 plates exhibit comparable, and the lowest drag, coefficients due to the jet's trajectory. The *P*7 and *P*11 plates display similar drag coefficients as highlighted in the inset of figure 2(*b*). A detailed discussion and basic modelling of the wake characteristics of the perforated plates is presented in § 3.3. The torque distribution in figure 2(*c*) reveals that the *P*1 plate had the largest torque, whereas the *P*4 and *P*11 plates had smaller values of T_z compared with the *P*7 case, even though the *P*1 and *P*4 plates exhibited lower drag. Figure 2 demonstrates that the perforations affect the drag and alter the drag distribution over the plates.

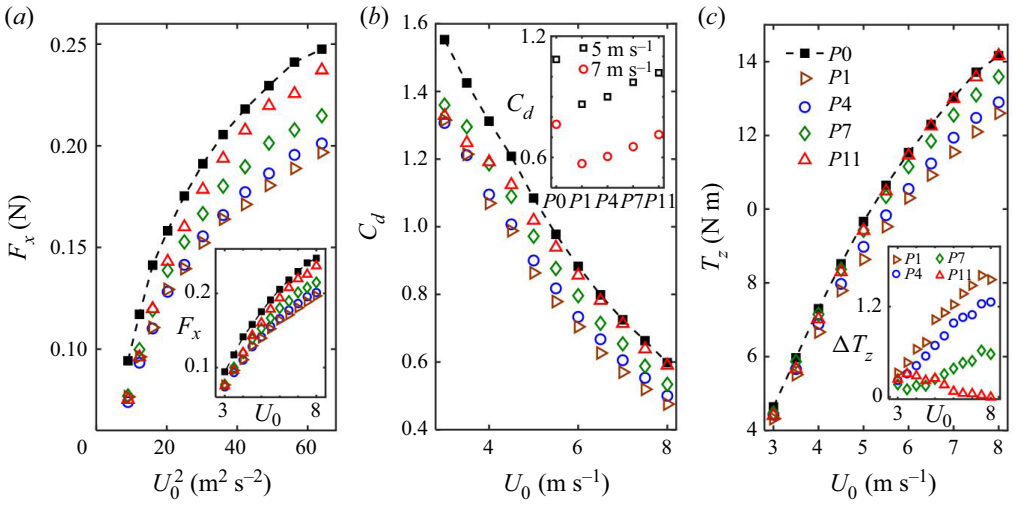

Figure 3. Effect of perforation location on selected flexible plates: $P1$ (brown ▷); $P4$ (blue ○); $P7$ (green ◇); $P11$ (red △); the solid $P0$ (■) flexible plate is included as reference. (*a*) Drag force, (*b*) drag coefficient and (*c*) base torque, T_z. The inset in (*b*) shows C_d variation for each plate at a fixed U_0, and the inset in (*c*) shows the torque difference between the base and perforated plates.

3.2. *Mean aerodynamic force and reconfiguration of flexible plates*

Here, we investigate the influence of various incoming velocities, namely the Cauchy number (Ca) and Reynolds number (Re) and relative perforation location on the reconfiguration and force coefficient of flexible plates. Although there was a general similarity in mean deformation across the plates under a given flow condition, discernible discrepancies in drag coefficients indicated that the position of the perforations has a critical impact on the plates' dynamics.

Figure 3 depicts the measured drag, torque and drag coefficient C_d for several flexible plates, namely $P0$ (solid), $P1$, $P4$, $P7$ and $P11$, with the flexible base plate exhibiting a negative Vogel exponent of $V \approx -0.8$. As illustrated in figure 3(*b*), the perforated plates display lower C_d values than the unperforated $P0$ base case. In fact, all perforated plates demonstrate a reduction in C_d, with this drag reduction being most prominent for plates with perforations at the root, i.e. the $P1$ plate. The C_d monotonically increases as the perforation moves towards the tip of the plate, which results in the minimum C_d reduction for the $P11$ case, as shown in the inset of figure 3(*b*). Notably, the difference in C_d between the perforated $P11$ and the unperforated base case becomes insignificant at a higher incoming velocity $U_0 > 7$ m s^{-1}, indicating that the distribution of drag is not solely dependent on plate stiffness and porosity. The location of the perforation orifice also plays a crucial role in determining drag, even though the plate has the same porosity in its non-deformed state. Thus, it is crucial to consider an effective porosity for different perforation locations under bending.

Figure 4 displays the drag coefficient obtained from both the experimental measurements and complementary direct numerical simulations (see the Appendix (A)), the latter including also the cases in which only the Cauchy number was varied while keeping the Reynolds number fixed at $Re = 10^3$. By combining the experimental and numerical results, we could examine a wider range of parameters and draw a conclusion on the significant role of the Cauchy number in controlling the reconfiguration and drag distribution of flexible plates, as previously reported in Luhar & Nepf (2011).

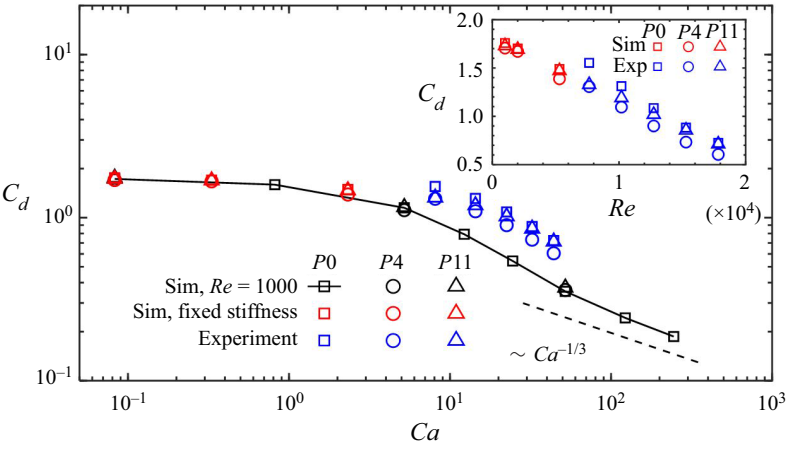

Figure 4. Drag coefficient, C_d, from experiments (blue) and numerical simulations (red), as a function of the Cauchy number, Ca. Black symbols show additional numerical results at a fixed $Re = 1000$. The inset shows C_d as a function of Re.

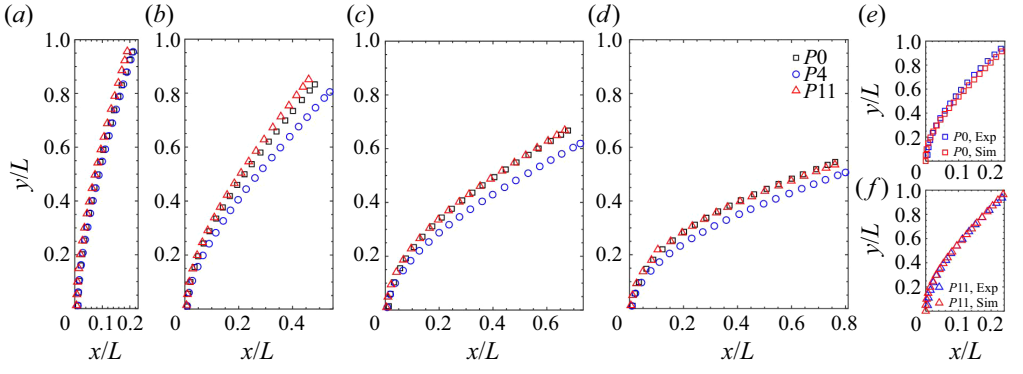

Figure 5. Measured reconfiguration of the $P4$ (blue ○) and $P11$ (red △) plates, with the solid $P0$ (□) plate as a reference, under $U_0 =$ (*a*) 2, (*b*) 4, (*c*) 6 and (*d*) 8 m s^{-1}. Comparisons between measurements and simulations at $Ca \approx 4$ are shown for the (*e*) $P0$ and (*f*) $P11$ plates. Note that (*e*,*f*) are stretched in the abscissa to aid comparison.

The measured reconfiguration of three representative plates $P0$ (unperforated), $P4$ and $P11$ at various incoming velocities is illustrated in figure 5. Additionally, figure 5(*e*,*f*) presents numerical results that enable direct comparison with experiments. Despite the small porosity resulting in similar deformation magnitudes for all plates, it is noteworthy that the plate with perforation at the base ($P1$) exhibited the largest deformation across the Ca range. In contrast, the plate with the perforation at the tip showed only minor changes compared with the base case at higher U_0 and a smaller deformation at lower incoming velocity. These differences in the mean plate deformation result from the combined effect of the local force and bending stiffness EI_{local} distributions along the plate. The lower torque experienced by $P11$ plate (figure 3*c*) resulted in a smaller deformation at comparatively low flow velocity, whereas plate $P11$ showed a similar torque as the $P0$ base case at relatively high flow velocity due to a diminishing effect of porosity, leading to a similar deformation to the base case $P0$.

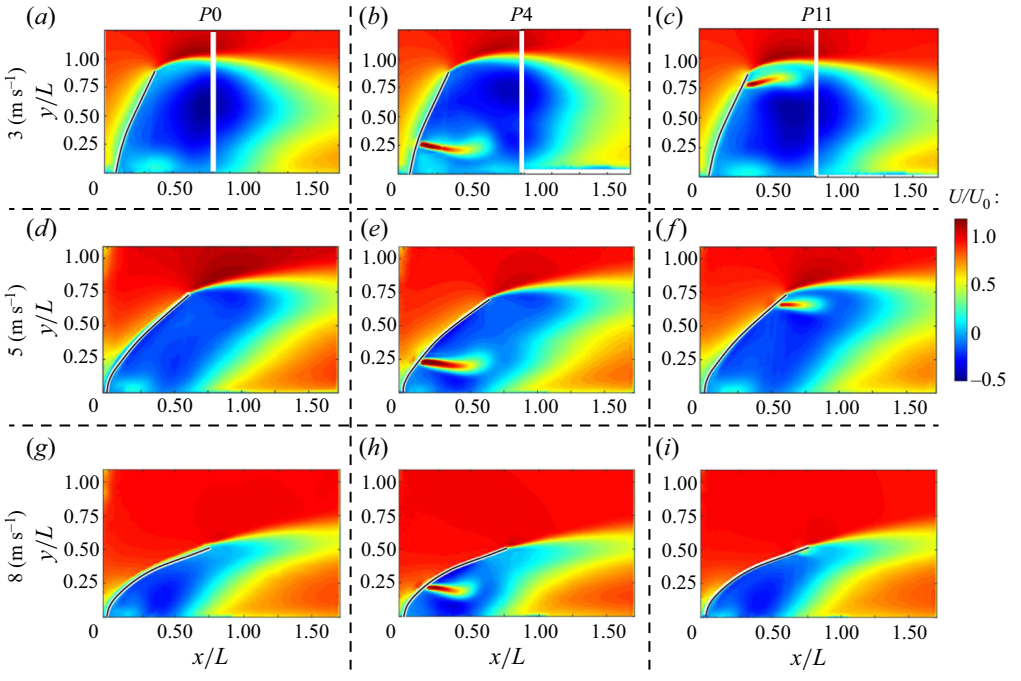

Figure 6. Measured time-averaged streamwise velocity fields around the *P*0 (solid), *P*4 and *P*11 flexible plates under $U_0 = 3$, 5 and 8 m s^{-1}. In (*a–c*), the white bar indicates the stitching edge of two PIV FOVs.

3.3. *Wake characteristics of flexible perforated plates*

To investigate the impact of perforation location on drag and structural deformation, the flow field near the plates was analysed for specific incoming flow velocities, $U_0 = 3$, 5 and 8 m s^{-1}, and perforation locations, plates P0 (solid), P4 and P11. The time-averaged streamwise velocity distribution is depicted in figure 6 for these cases. The presence of a jet-like structure emanating from the perforation is a crucial factor responsible for altering the wake of the plates. It should be noted that the low porosity of the perforations ($\gamma \approx 0.028$) resulted in minimal changes to the backward flow region where $U(x, y) < 0$, in contrast to the significant backward flow region reduction observed in plates with high porosity (Jin *et al.* 2020).

Basic characterization of a jet's structure involves an assessment of the spatial features of the jet centre, the time-averaged profile of the streamwise velocity along the centreline (U_c), and the evolution of the time-averaged streamwise velocity's spanwise distribution at various downwind locations. These provide insight into the effects of the jet on the plate. The wake features are depicted in figure 7. The size of the jet is comparable to $2b_0$, which represents the width of the perforation, as illustrated in figure 7(*d*). On closer examination of the time-averaged streamwise velocity, as shown in figure 7(*b*), the jet centreline is curved, and the line of maximum velocity is denoted in black. The spanwise turbulence intensity is displayed in figure 7(*c*), where the red-dashed box denotes a low turbulence potential core that extends over a distance of x_c. A corresponding conceptual sketch is presented in figure 7(*d*).

Figure 8 illustrates the distributions of normalized velocity for the jet centre, U_c/U_0, for the *P*4 and *P*11 plates at various incoming flow velocities. The velocity profiles exhibit typical characteristics of a turbulent jet centreline, with a relatively constant

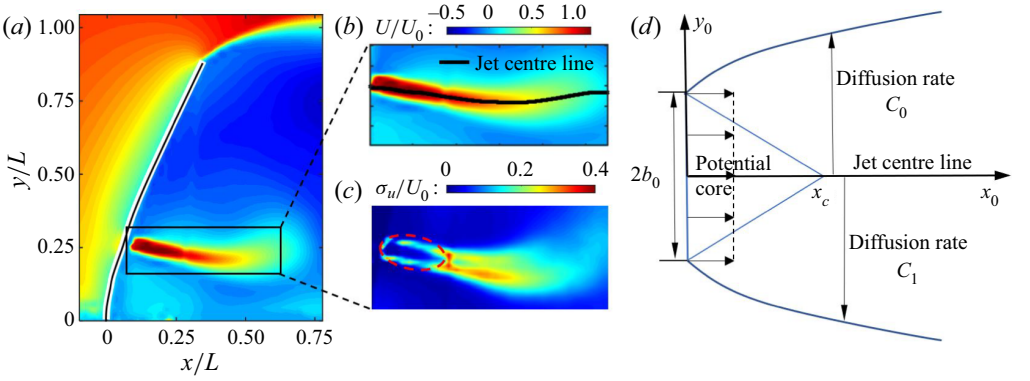

Figure 7. (*a*) Characteristics of the measured jet through the perforation in the *P*4 plate under $U_0 = 3$ m s^{-1}. (*b*) Mean streamwise velocity, U/U_0. The black line indicates the jet centre. (*c*) Streamwise turbulence intensity, σ_u/U_0. The red-dashed box shows the potential core. (*d*) Conceptual diagram of the jet.

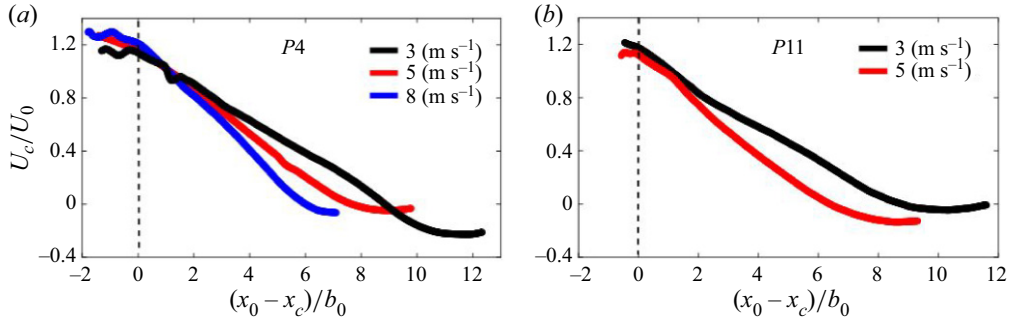

Figure 8. Measured jet centre velocity, U_c/U_0, for the (*a*) *P*4, and (*b*) *P*11 flexible plates.

velocity within the potential core and a linear decrease downstream, as described in Pope (2000). In contrast to the constant gradient for water jet velocities (Giralt, Chia & Trass 1977; Rajaratnam, Zhu & Rai 2010; Shademan, Balachandar & Barron 2013), current measurements show that the slope varies between cases with U_0 and perforation location. At low U_0, a lower normalized velocity is evident within the potential core, while the centreline profile decays faster outside the potential core at higher U_0, with U_c/U_0 approaches zero at a shorter distance $(x - x_c)/b_0$ from the potential core, leading to a shorter bulk jet. Moreover, a comparison of jet profiles for different perforation locations at the same U_0 in figure 8(*a*,*b*) suggests a shorter jet length for the perforation located near the tip, i.e. the *P*11 plate.

A possible way to characterize the influence of incoming velocity and perforation location on the distribution of the jet centreline velocity U_c could be through a single parameter. Figure 9 presents the normalized U_c by the corrected incoming velocity $U_0 \cos\theta$ and corrected perforation half-width $b_0 \cos\theta$, where these quantities are determined as the U_0 component perpendicular to the perforation and the projected b_0 in the streamwise direction. This first attempt results in a similar normalized jet length $(x - x_c)/b_0 \cos\theta$ for all cases; however, it further deviates the normalized exit velocity at $(x - x_c) = 0$.

Inspection of scaling with velocity U_0 appears inappropriate for representing U_c profiles. This is because the flow near the structures is significantly affected by the

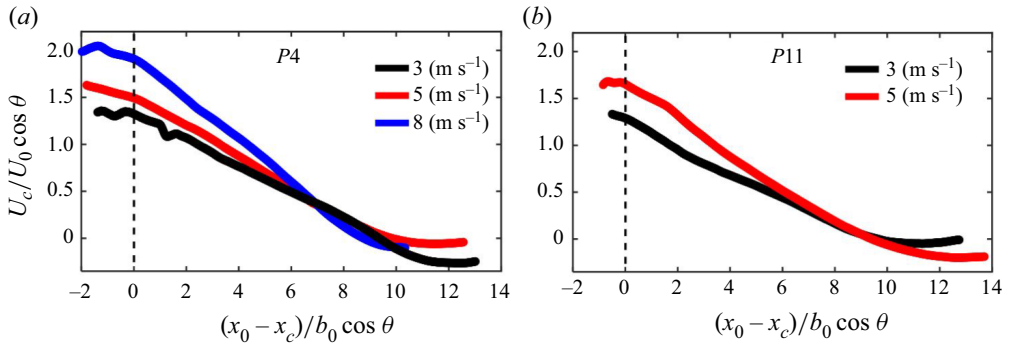

Figure 9. Measured jet centre velocity normalized by corrected incoming velocity, $U_c/(U_0\cos\theta)$ with normalized distance by effective perforation half-width, $(x - x_c)/(b_0\cos\theta)$, for the (*a*) *P*4, and (*b*) *P*11 plates.

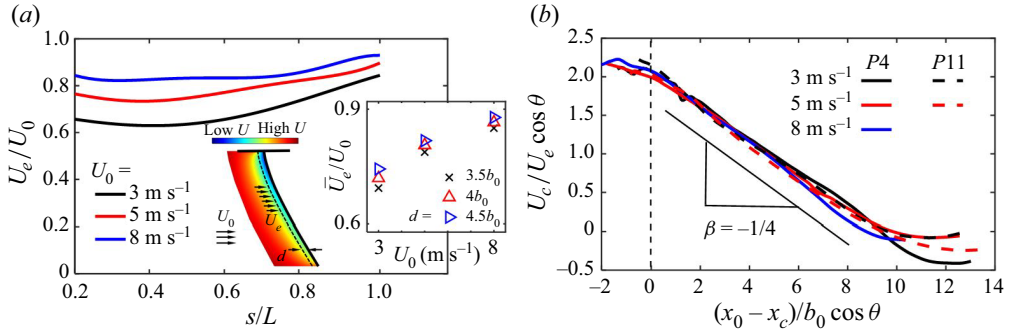

Figure 10. (*a*) Measured effective velocity, U_e, at $d/b_0 = 4$ from the *P*4 plate for $U_0 = 3$, 5 and 8 m s^{-1}; the dashed line in the schematic illustrates the location used for the effective velocity, and the inset shows spatially averaged U_e at $d/b_0 = -3.5$, -4 and -4.5. (*b*) Renormalized centre jet centrevelocity, $U_c/(U_e\cos\theta)$, with normalized distance by effective perforation half-width $(x - x_c)/(b_0\cos\theta)$.

windward side of the body (Hemmati, Wood & Martinuzzi 2016; Liu *et al.* 2017; Jin *et al.* 2020), making it crucial to consider the effective velocity U_e at the perforation. Here, U_e is defined as the velocity experienced in the proximity of the perforation at a location $d/b_0 = 4$ upwind of the front surface of the plate (Jin *et al.* 2020). To assess the influence of the effective velocity, figure 10(*a*) illustrates the distribution of U_e for the *P*4 plate at various U_0. As U_0 increases, the U_e/U_0 ratio also increases, mainly due to the higher plate deformation, as depicted in figure 5. Furthermore, the plate near the tip is more streamlined than its root, resulting in a higher U_e. The inset of figure 10(*a*) displays the spatially averaged U_e along the plate arclength, s, at various upwind locations $d/b_0 = 3.5 - 4.5$, revealing a similar distribution. The use of the corrected effective velocity, $U_e\cos\theta$, and corrected perforation half-width, $b_0\cos\theta$, to normalize U_c in figure 9 allows the profiles at different U_0 and perforation locations to collapse onto an approximately linear trend with a slope of $\beta = -1/4$ for $x > x_c$. This suggests that the distribution of U_c is a function of the effective local velocity and local bending angle and can be expressed as $U_c = f(U_e, \theta) \approx -0.25(x - x_c)U_e/b_0 + 2.05(U_e\cos\theta)$.

Transverse jet profiles are shown in figure 11(*a*,*c*), with the *P*4 plate at $U_0 = 8$ m s^{-1} and the *P*11 plate at $U_0 = 3$ m s^{-1} serving as examples. The profiles display dissimilar diffusion rates for the upper, $y - y_0 > 0$, and lower, $y - y_0 < 0$, sections of the jets, with slower diffusion at $(y - y_0)/b_0 < 0$ for the *P*4 plate subjected to 8 m s^{-1} flow, due to the

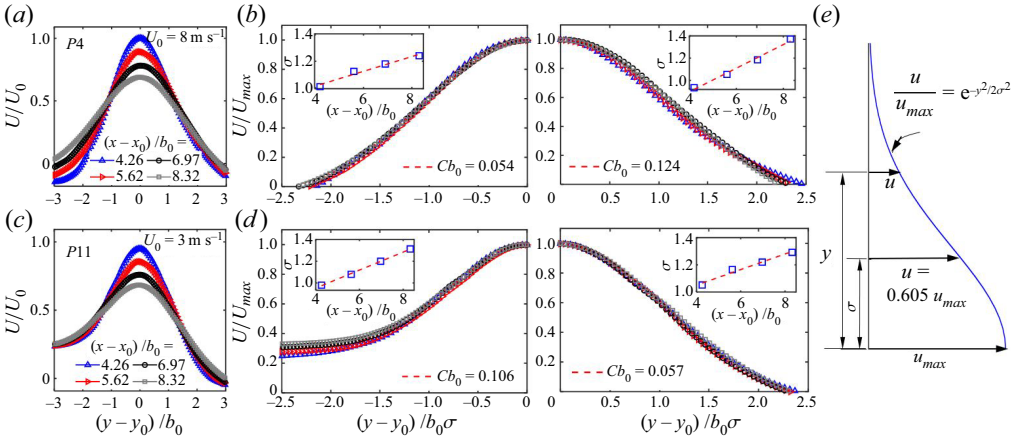

Figure 11. Selected transverse profiles of time-averaged streamwise velocity of the jets through perforations from numerical simulations: (*a*) *P*4 plate, $U_0 = 8$ m s^{-1}; (*b*) normalized profiles; (*c*) *P*11 plate, $U_0 = 3$ m s^{-1}; (*d*) normalized profiles; (*e*) Schematics of a Gaussian distribution. Here σ denotes the distance where $U/U_{max} = 0.605$. Insets show the σ with distance.

lower turbulence levels, similar to those presented in figure 7(*c*). Despite these differences, both jet segments exhibit self-similar characteristics as they progress downwind, as shown in figure 11(*b*,*d*), conforming to the standard Gaussian distribution

$$\frac{u}{u_{max}} = \exp\left(-\frac{y^2}{2\sigma^2}\right), \tag{3.2}$$

where σ is the standard deviation. Additionally, the condition of dynamic similarity is satisfied as indicated by Albertson *et al.* (1950), leading to a constant diffusion angle such that

$$(x - x_0)/\sigma = C. \tag{3.3}$$

The inset of figure 11(*b*,*d*) illustrates the σ evolution at various downwind distances and yields the diffusion rate C, which indicates a higher value for the upper side jet that is approximately twice the value for the bottom side counterpart. This result provides evidence that the local shear (or turbulence intensity) outside of the potential core influences C, such that $C = f(\sigma_u)$, where f is an empirical function fitted to the current experimental data. Given the information about U_c and C, and assuming a linear decay of potential core width from $w = 2b_0$ at $x = x_0$ to zero at $x = x_0 + x_c$, the predicted velocity profiles of the empirical model are shown in figure 12 as a red-dashed line for various downwind locations. The semiempirical modelled profiles agree well with the experimental data represented by the blue circles.

Further analysis through numerical simulations allowed for the investigation of the jet centreline trajectory, jet centreline profiles and the effective velocity distribution at a fixed Reynolds number of $Re = 1000$ (which is one order of magnitude lower than the experimental cases), allowing us to separate the Reynolds and Cauchy number influences. By adjusting the blade's stiffness, we simulated three Cauchy numbers of $Ca = 0.1$, 7 and 75, thus spanning a wider range for this parameter.

Figure 13 displays a similar streamwise velocity pattern observed in the simulations if compared with the experimental results (shown in figure 6). The jet centreline profiles' collapse in figure 14 confirms that Ca is the dominant parameter, while the jet centreline

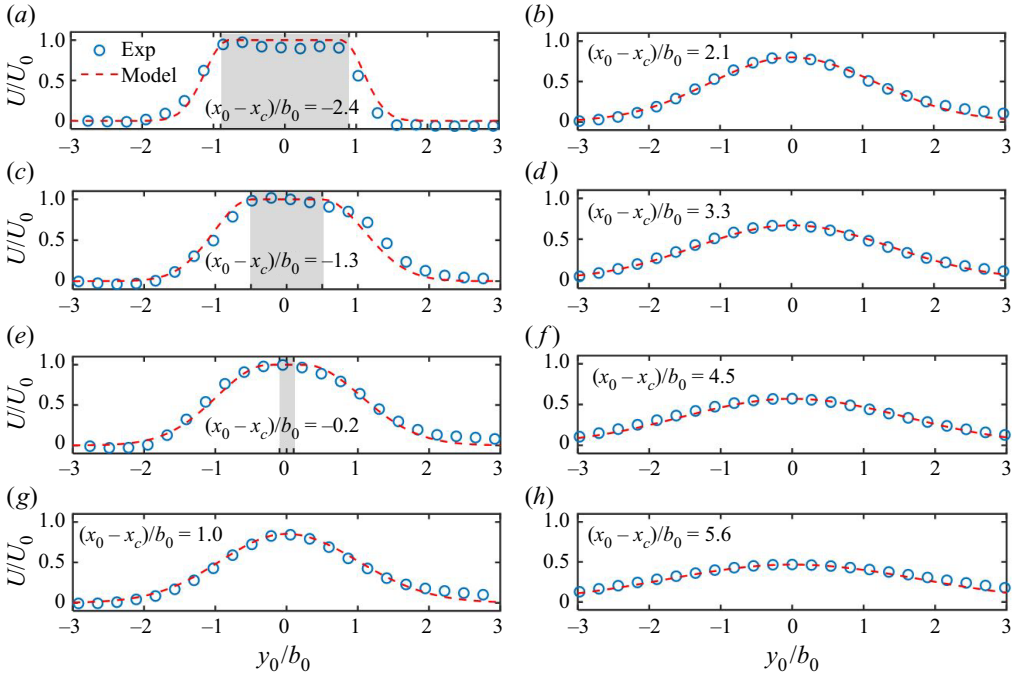

Figure 12. Comparison between experimental (blue ○) and modelled (red – –) transverse jet profiles from the perforations at various downwind locations for the plate $P4$ under $U_0 = 3$ m s^{-1}. The grey area denotes the potential core region.

velocity demonstrates independence from the Reynolds number for $Re \in [0.1, 3.4] \times 10^4$. Moreover, the centreline trajectory is primarily a function of Ca and perforation location as it is affected by the wake recirculation zones, as shown in figure 15(a), which depicts streamlines in the wake of the $Ca = 0.1$ base plate without perforation. The jet centreline trajectory also allows us to define an exit angle of the jet, α, as shown in figure 15(b). The subsequent section will provide additional insight into how this exit angle α affects the local jet thrust, consequently impacting the plate's bulk drag.

3.4. *A first-order formulation for drag in perforated plates*

As a basic estimation, figure 6 demonstrates that the total drag on the plate can be partitioned into two distinct constituents: namely, the drag acting solely on the plate and the force change by the perforation as

$$C_d \approx C_{d,P0} - C_{T,jet}. \tag{3.4}$$

The presence of the jet induces modifications in the local thrust, which can be computed by carrying out a momentum integral over a control volume that encloses the jet. Then, the force coefficient C_F can be estimated based on this value as

$$C_F = \frac{2b}{A} \int_{-H}^{+H} \frac{U(y)}{U_\infty} \left(\frac{U(y)}{U_\infty} - 1 \right) \mathrm{d}y. \tag{3.5}$$

Typically, the selection of $U(y)$ and H in the momentum integral is based on the premise that they are sufficiently far away from the perforated plate to render the contribution

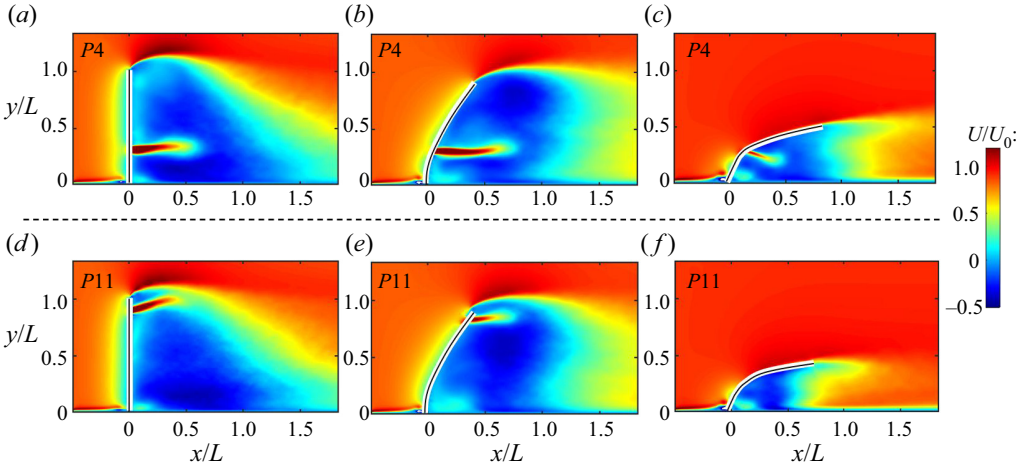

Figure 13. Time-averaged streamwise velocity field at $z = 0$ around the (*a–c*) *P*4 and (*d–f*) *P*11 plates at $Ca = 0.1$, 7 and 75 for $Re = 1000$ from numerical simulations.

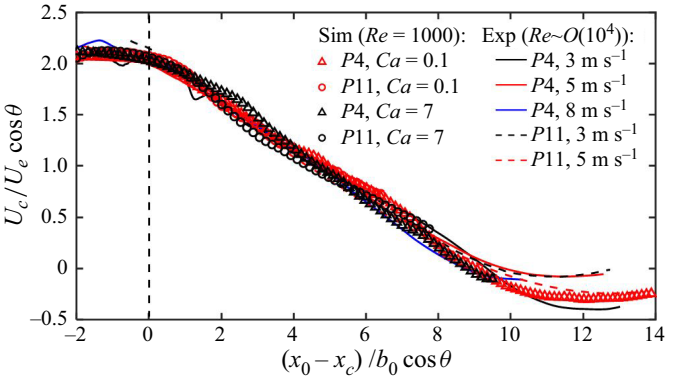

Figure 14. Normalized jet centre velocity, $U_c/U_e \cos\theta$, with normalized downwind distance, $(x_0 - x_c)/b_0 \cos\theta$, for various *Ca* and *Re* using numerical simulations and experiments.

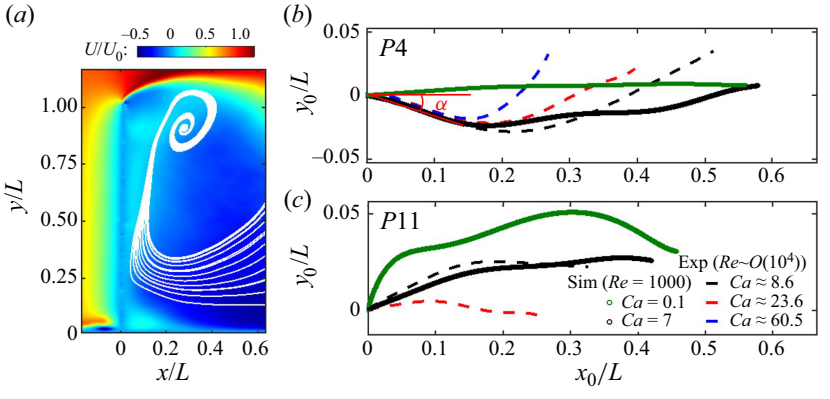

Figure 15. (*a*) Time-averaged streamwise velocity distribution around the *P*0 (solid) plate at $Ca = 0.1$ from simulation; white curves denote streamlines highlighting the recirculation region. Jet centreline trajectories for the (*b*) *P*4 and (*c*) *P*11 plates for various *Ca*.

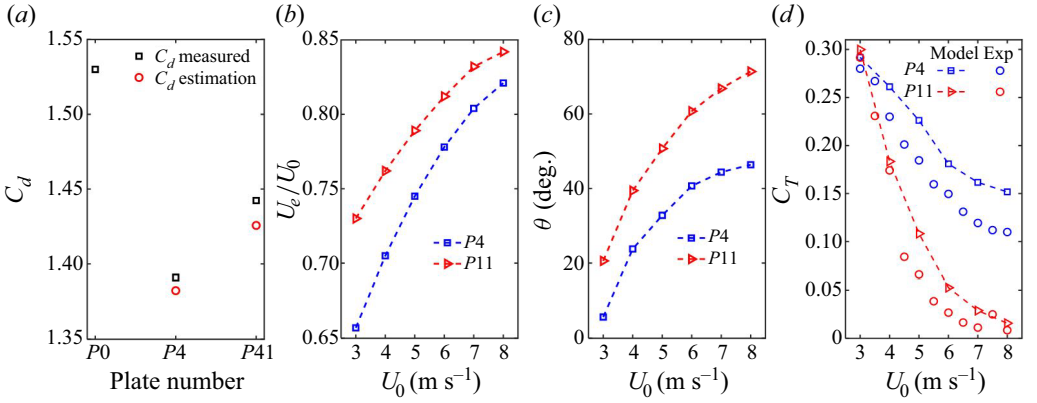

Figure 16. (*a*) Comparison of measured and modelled C_d for rigid plates under $U_0 = 3$ m s^{-1}, (*b*) measured Ue/U_0 for the *P*4 and *P*11 flexible plates, (*c*) measured local bending angle, θ, (*d*) measured and estimated local jet thrust coefficient, C_T, for the *P*4 and *P*11 flexible plates. The dashed line represents the estimation using a default $\gamma_{3D} = 1$.

of pressure and velocity fluctuations negligible in the integrand (Ramamurti & Sandberg 2001; Bohl & Koochesfahani 2009). However, due to the proximity of the perforations to the shear layer and the wake generated by the plate, disentangling the impact of pressure and velocity fluctuations between the jet and wake becomes challenging for the far downstream $U(y)$ profile. Therefore, $U(y)$ profiles in the vicinity of the perforation (i.e. $x_0 = 0^+$) are selected for the momentum integral, where the contribution of the jet passing through the perforation dominates, and $H = b_0$ is chosen for integration. This selection yields a uniform velocity profile with a width of $2b_0$, exhibiting minimal velocity fluctuations within the potential core, as depicted in figures 7(*c*) and 12. The estimation of thrust is expressed as

$$\left.\begin{array}{c} T_{jet,model} \propto \dot{m} U_{c,x=0} \cos\alpha \propto \rho A U_e^2 \cos^2\theta \cos\alpha = \gamma_{3D} \rho A U_e^2 \cos^2\theta \cos\alpha, \\ C_{T_{jet,model}} = T_{jet,model}/(\tfrac{1}{2}\rho_f U_0^2 A),\ C_{T_{jet,exp}} \approx C_{d_{P0}} - C_{d_{P_i}}, \end{array}\right\} \tag{3.6}$$

where α is the exit angle of the jet obtained from the jet centreline trajectory in figure 15(*b*,*c*). The coefficient γ_{3D} takes into consideration geometry-dependent factors that account for three-dimensional wake effects. In the case of rigid plates, the ratio U_e/U_0 remains constant across a broad range of U_0, and $\cos\theta = 1$. The difference in force between the plates is directly proportional to $\cos\alpha$. As depicted in figure 16(*a*), the measured and estimated C_d values are compared using (3.6). The *P*4 case exhibits a nearly straight centreline, resulting in the highest local thrust and, therefore, the lowest total drag. An upward tilting trajectory results in larger α values for the *P*11 plate, resulting in a smaller C_d.

The experimental trends of U_e/U_0 and θ obtained from the experiments are employed in (3.6) to estimate the total drag of the flexible plates, as illustrated in figure 16(*b*,*c*). Figure 16(*d*) compares the modelled local jet thrust coefficient C_T and the measured values. The experimental C_T are computed by subtracting the drag coefficient of the perforated plates $C_{d,Pi}$ from the base plate drag coefficient $C_{d,P0}$ provided in (3.6). The predicted C_T obtained using a default $\gamma_{3D} = 1$ yields a higher value than the experimental measurement of C_T. The observed deviation in thrust within the simple model can be attributed to two primary factors. First, three-dimensional effects play a varying role.

Second, as the Re increases, the accuracy of the basic jet thrust estimation diminishes. This discrepancy arises from the omission of pressure and velocity fluctuation terms in the momentum balance, resulting in an overestimation of the jet thrust. Although the model overlooks the downwind momentum adjustment, it captures the general trend of how the perforations affect the drag of the flexible plates, taking into account the various perforation locations and U_0. The value of C_T estimated through (3.6) indicates the effective porosity of the flexible structures with square perforations at a particular Ca since both the plate reconfiguration and U_e are functions of the Cauchy number. The impact of the perforation reduces with the growth of U_0 (Ca), owing to an increase in θ. The location of the perforation dictates the reduction rate of such effective porosity, with perforations positioned closer to the tip exhibiting a substantially higher reduction rate in C_T. The C_T values for $P4$ and $P11$ are nearly identical at $U_0 \approx 3$ m s^{-1}, but $P11$ experiences a much sharper decay for $U_0 \leq 5$ m s^{-1}. Furthermore, both $P4$ and $P11$ cases exhibit a slower reduction rate of C_T for $U_0 > 5$ m s^{-1} as θ increases marginally after a sufficient amount of bending experienced by the flexible plates.

4. Remarks and conclusions

Our study provides a comprehensive analysis of the influence of localized perforations on the dynamics of flexible plates subjected to uniform flow conditions with negligible turbulence. By conducting wind-tunnel experiments and direct numerical simulations, we investigated a wide range of parameters, including the perforation location, Cauchy and Reynolds numbers. We systematically observed a trend in the plate reconfiguration, the wake of the perforated plates and the corresponding aerodynamic force. The wake of perforated plates is characterized by a jet-like structure passing through the perforation orifice, and we modelled this jet by scaling its centreline velocity with a corrected effective local velocity, $U_e \cos\theta$, and its length scale with the corrected half-width of perforation, $b_0 \cos\theta$.

Additionally, we propose a first-order formulation for estimating the bulk drag of perforated plates as the drag of the unperforated base plate minus the thrust generated by the jet passing through the perforation orifice. This jet thrust decreases as U_0 increases due to an increase in local bending angle, θ, illustrating how effective porosity decreases as Ca increases. Our results may have implications for the aeroelastic characterization of flexible structures with non-homogeneous, localized porosity, a relatively underexplored topic with potential relevance to many engineering applications. Our study also establishes a fundamental basis for further research focusing on other geometrical features, such as different perforation shapes or sizes and flow regimes. Such studies would enhance our understanding of the complex interaction between flow and structures with low porosity and could facilitate the design of flexible structures with improved aerodynamic performance.

Acknowledgements. S.O. and M.E.R. acknowledge F. Viola for sharing the simulation code and the computational resources on the Saion cluster provided by the Scientific Computing section of the Research Support Division at OIST. The Okinawa Institute of Science and Technology Graduate University (OIST) supported the two authors with subsidy funding from the Cabinet Office, Government of Japan.

Funding. S.O. is also supported by grant FJC2021-047652-I funded by MCIN/AEI/10.13039/501100011033 and European Union NextGenerationEU/PRTR.

Declaration of interests. The authors report no conflict of interest.

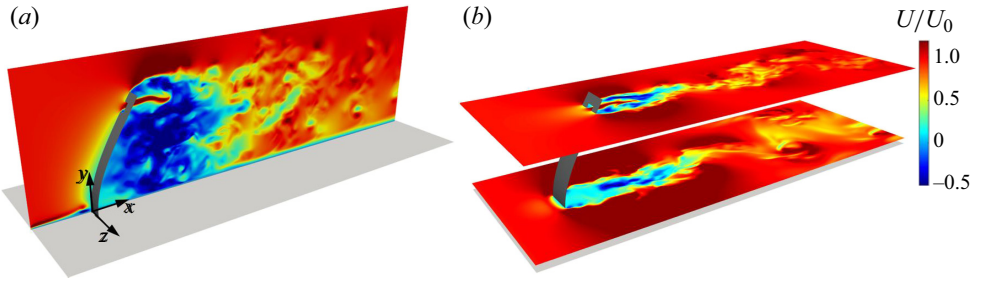

Figure 17. Numerical simulation snapshot of case $P11$ at $Re = 1000$ and $Ca \approx 7$, showing (a) a wall-normal plane at $z = 0$ and (b) two horizontal planes colouredby instantaneous streamwise velocity – one passing through the perforation and the other slightly above the plate root. The grey horizontal plane indicates the solid boundary.

Author ORCIDs.
Shyuan Cheng https://orcid.org/0000-0001-8563-9054;
Stefano Olivieri https://orcid.org/0000-0002-7795-6620;
Marco E. Rosti https://orcid.org/0000-0002-9004-2292;
Leonardo P. Chamorro https://orcid.org/0000-0002-5199-424X.

Appendix A. Numerical study

A computational investigation was carried out to complement the experimental range and to explore the three-dimensional flow field, enabling the examination of lower Reynolds numbers (i.e. $Re \lesssim 5 \times 10^3$) and the separation of the effects of the primary dimensionless governing parameters, specifically Reynolds and Cauchy numbers.

We employed the in-house flow–structure interaction solver AFiD (Viola *et al.* 2022). The code is based on the fractional-step method that solves the incompressible Navier–Stokes equations, (second-order) centred finite-difference for spatial discretization and (second-order) Adams–Bashforth and Crank–Nicolson scheme for temporal discretization of the nonlinear and diffusive terms, respectively (Viola, Meschini & Verzicco 2020; Viola *et al.* 2022). An immersed boundary method, based on a direct forcing and moving least-squares interpolation (de Tullio & Pascazio 2016), is used to model the flow–structure interaction and indirectly impose the no-slip boundary condition between the fluid and the solid surface. The structural dynamics of the elastic structures is solved using a spring-network model for thin membranes (Viola *et al.* 2020). The computational framework has been validated in a variety of flow–structure interaction test cases (de Tullio & Pascazio 2016; Olivieri *et al.* 2021).

The chosen computational domain is a box of size $L_x/b = 16$, $L_y/b = 8$ and $L_z/b = 6$ along the streamwise, wall-normal (vertical) and spanwise directions, with the origin of the reference frame coinciding with the midpoint of plate root. The inlet of the domain lies at $x/b = -2$, at which a Dirichlet condition imposing uniform velocity is applied, while a convective boundary condition is used at the outlet ($x/b = 14$). The no-slip condition applies at the bottom ($y = 0$) and top ($y = L_y$) boundary, whereas periodic conditions apply over the lateral boundaries $z = \pm L_z/2$. The domain is discretized with a uniform grid spacing $\Delta/b \approx 0.027$. Negligible differences in the main quantities of interest (e.g. plate deformation, aerodynamic forces and characteristic frequencies of motion) were found when increasing the domain size and numerical resolution.

The simulations considered the same plate geometries as the experiments and focused on cases where the perforations were located at positions $P4$ or $P11$ and the unperforated

case (*P*0). To facilitate direct comparison between the experimental and numerical results, the simulations first addressed the lowest incoming flow velocity tested in the wind tunnel, which was $U_0 = 2$ m s^{-1}. Subsequently, two additional cases were simulated at lower Reynolds numbers, with plate relative flexibility (i.e. Cauchy number) varied in proportion to the change in wind velocity. Finally, a series of simulations were conducted at a fixed Reynolds number of 10^3, with the Cauchy number varied over nearly four orders of magnitude, ranging from approximately 10^{-1} to 3×10^2. A representative snapshot from one of the performed runs is given in figure 17.

References

Alben, S., Shelley, M. & Zhang, J. 2002 Drag reduction through self-similar bending of a flexible body. *Nature* **420** (6915), 479–481.

Alben, S., Shelley, M. & Zhang, J. 2004 How flexibility induces streamlining in a two-dimensional flow. *Phys. Fluids* **16** (5), 1694–1713.

Albertson, M., Dai, Y., Jensen, R. & Rouse, H. 1950 Diffusion of submerged jets. *Trans. Am. Soc. Civ. Engrs* **115** (1), 639–664.

Barry, O.R. & Tanbour, E.Y. 2018 Resonant frequencies of perforated plates with rectangular slots. *Proc. Inst. Mech. Engrs C: J. Mech. Engng Sci.* **232** (7), 1247–1254.

Basnet, K. & Constantinescu, G. 2017 The structure of turbulent flow around vertical plates containing holes and attached to a channel bed. *Phys. Fluids* **29** (11), 115101.

Betz, A. 1920 Das maximum der theoretisch möglichen ausnutzung des windes durch windmotoren. *Z. Ges. Turbinenwesten* **20**.

Bitog, J., Lee, I.-B., Hwang, H.-S., Shin, M.-H., Hong, S.-W., Seo, I.-H., Mostafa, E. & Pang, Z. 2011 A wind tunnel study on aerodynamic porosity and windbreak drag. *Forest Sci. Technol.* **7** (1), 8–16.

Bohl, D.G. & Koochesfahani, M.M. 2009 MTV measurements of the vortical field in the wake of an airfoil oscillating at high reduced frequency. *J. Fluid Mech.* **620**, 63–88.

Castro, I. 1971 Wake characteristics of two-dimensional perforated plates normal to an air-stream. *J. Fluid Mech.* **46** (3), 599–609.

Cummins, C., Seale, M., Macente, A., Certini, D., Mastropaolo, E., Viola, I.M. & Nakayama, N. 2018 A separated vortex ring underlies the flight of the dandelion. *Nature* **562** (7727), 414–418.

Dong, Z., Luo, W., Qian, G., Lu, P. & Wang, H. 2010 A wind tunnel simulation of the turbulence fields behind upright porous wind fences. *J. Arid. Environ.* **74** (2), 193–207.

Dong, Z., Luo, W., Qian, G. & Wang, H. 2007 A wind tunnel simulation of the mean velocity fields behind upright porous fences. *Agric. Forest Meteorol.* **146** (1–2), 82–93.

Farisenkov, S.E., Lapina, N.A., Petrov, P.N. & Polilov, A.A. 2020 Extraordinary flight performance of the smallest beetles. *Proc. Natl Acad. Sci.* **117** (40), 24643–24645.

Giralt, F., Chia, C.-J. & Trass, O. 1977 Characterization of the impingement region in an axisymmetric turbulent jet. *Ind. Engng Chem. Fundam.* **16** (1), 21–28.

Gosselin, F., De Langre, E. & Machado-Almeida, B. 2010 Drag reduction of flexible plates by reconfiguration. *J. Fluid Mech.* **650**, 319–341.

Guan, D., Zhang, Y. & Zhu, T. 2003 A wind-tunnel study of windbreak drag. *Agric. Forest Meteorol.* **118** (1–2), 75–84.

Guttag, M., Karimi, H.H., Falcón, C. & Reis, P.M. 2018 Aeroelastic deformation of a perforated strip. *Phys. Rev. Fluids* **3** (1), 014003.

Harder, D.L., Speck, O., Hurd, C.L. & Speck, T. 2004 Reconfiguration as a prerequisite for survival in highly unstable flow-dominated habitats. *J. Plant Growth Regul.* **23**, 98–107.

Hemmati, A., Wood, D.H. & Martinuzzi, R.J. 2016 Characteristics of distinct flow regimes in the wake of an infinite span normal thin flat plate. *Intl J. Heat Fluid Flow* **62**, 423–436.

Hong, L., Cheng, S., Houseago, R.C., Parsons, D.R., Best, J.L. & Chamorro, L.P. 2022 On the submerged low-Cauchy-number canopy dynamics under unidirectional flows. *J. Fluids Struct.* **113**, 103646.

Ibrahim, T.K., Al-Sammarraie, A.T., Al-Jethelah, M.S., Al-Doori, W.H., Salimpour, M.R. & Tao, H. 2020 The impact of square shape perforations on the enhanced heat transfer from fins: experimental and numerical study. *Intl J. Therm. Sci.* **149**, 106144.

Jin, Y., Kim, J.-T., Cheng, S., Barry, O. & Chamorro, L.P. 2020 On the distinct drag, reconfiguration and wake of perforated structures. *J. Fluid Mech.* **890**, A1.

Koo, J.-K. & James, D.F. 1973 Fluid flow around and through a screen. *J. Fluid Mech.* **60** (3), 513–538.

LECLERCQ, T. & DE LANGRE, E. 2016 Drag reduction by elastic reconfiguration of non-uniform beams in non-uniform flows. *J. Fluids Struct.* **60**, 114–129.

LEE, S.-J. & KIM, H.-B. 1999 Laboratory measurements of velocity and turbulence field behind porous fences. *J. Wind Engng Ind. Aerodyn.* **80** (3), 311–326.

LIU, B., HAMED, A., JIN, Y. & CHAMORRO, L. 2017 Influence of vortical structure impingement on the oscillation and rotation of flat plates. *J. Fluids Struct.* **70**, 417–427.

LUHAR, M. & NEPF, H. 2011 Flow-induced reconfiguration of buoyant and flexible aquatic vegetation. *Limnol. Oceanogr.* **56** (6), 2003–2017.

LUSCHI, L. & PIERI, F. 2014 An analytical model for the determination of resonance frequencies of perforated beams. *J. Micromech. Microengng* **24** (5), 055004.

OLIVIERI, S., VIOLA, F., MAZZINO, A. & ROSTI, M.E. 2021 Direct numerical simulation of flapping flags in grid-induced turbulence. *Phys. Fluids* **33** (8), 085116.

POPE, S.B. 2000 *Turbulent Flows*. Cambridge University Press.

RAJARATNAM, N., ZHU, D.Z. & RAI, S. 2010 Turbulence measurements in the impinging region of a circular jet. *Can. J. Civ. Engng* **37** (5), 782–786.

RAMAMURTI, R. & SANDBERG, W. 2001 Simulation of flow about flapping airfoils using finite element incompressible flow solver. *AIAA J.* **39** (2), 253–260.

SANTHANAKRISHNAN, A., ROBINSON, A.K., JONES, S., LOW, A.A., GADI, S., HEDRICK, T.L. & MILLER, L.A. 2014 Clap and fling mechanism with interacting porous wings in tiny insect flight. *J. Expl Biol.* **217** (21), 3898–3909.

SHADEMAN, M., BALACHANDAR, R. & BARRON, R.M. 2013 CFD analysis of the effect of nozzle stand-off distance on turbulent impinging jets. *Can. J. Civ. Engng* **40** (7), 603–612.

SINGH, A. & NARASIMHAMURTHY, V.D. 2022 Perforation effects on the wake dynamics of normal flat plates. *J. Fluid Mech.* **947**, A23.

STANFORD, B., IFJU, P., ALBERTANI, R. & SHYY, W. 2008 Fixed membrane wings for micro air vehicles: experimental characterization, numerical modeling, and tailoring. *Prog. Aerosp. Sci.* **44** (4), 258–294.

STEIROS, K. & HULTMARK, M. 2018 Drag on flat plates of arbitrary porosity. *J. Fluid Mech.* **853**, R3.

TAYLOR, G.I. 1952 Analysis of the swimming of long and narrow animals. *Proc. R. Soc. Lond* A*, Math. Phys. Sci.* **214** (1117), 158–183.

DE TULLIO, M.D. & PASCAZIO, G. 2016 A moving-least-squares immersed boundary method for simulating the fluid–structure interaction of elastic bodies with arbitrary thickness. *J. Comput. Phys.* **325**, 201–225.

TUNNICLIFFE, V. 1982 The effects of wave-induced flow on a reef coral. *J. Exp. Mar. Biol. Ecol.* **64** (1), 1–10.

VIOLA, F., MESCHINI, V. & VERZICCO, R. 2020 Fluid–structure-electrophysiology interaction (FSEI) in the left-heart: a multi-way coupled computational model. *Eur. J. Mech.*-B/*Fluids* **79**, 212–232.

VIOLA, F., SPANDAN, V., MESCHINI, V., ROMERO, J., FATICA, M., DE TULLIO, M.D. & VERZICCO, R. 2022 FSEI-GPU: GPU accelerated simulations of the fluid–structure–electrophysiology interaction in the left heart. *Comput. Phys. Commun.* **273**, 108248.

VOGEL, S. 1984 Drag and flexibility in sessile organisms. *Am. Zool.* **24** (1), 37–44.

VOGEL, S. 2009 Leaves in the lowest and highest winds: temperature, force and shape. *New Phytol.* **183** (1), 13–26.

VOLLSINGER, S., MITCHELL, S.J., BYRNE, K.E., NOVAK, M.D. & RUDNICKI, M. 2005 Wind tunnel measurements of crown streamlining and drag relationships for several hardwood species. *Can. J. Forest Res.* **35** (5), 1238–1249.